ELSEVIER

Soil Dynamics and Earthquake Engineering 28 (2008) 212–222

SOIL DYNAMICS AND EARTHQUAKE ENGINEERING

www.elsevier.com/locate/soildyn

A note on strength-reduction factors for design of structures near earthquake faults

Reza S. Jalali[a], Mihailo D. Trifunac[b,*]

[a]Department of Civil Engineering, Faculty of Engineering, University of Guilan, P.O. Box 3756, Rasht, Iran
[b]Deptartment of Civil Engineering, University of Southern California, Los Angeles, CA 90089, USA

Received 30 July 2006; accepted 12 June 2007

Abstract

Strength-reduction factors are analyzed for simplified near-fault, fault-normal and fault-parallel strong-motion displacements. It is shown that the common design rules for selection of the strength-reduction factors are conservative and properly describe the reduction amplitudes near faults of strong earthquakes, for fault-normal pulses. However, for fault-parallel displacements, the same reduction factors are not conservative and should be changed. It is recommended that for design close to active faults, the strength-reduction factors for all components of motion should be constant for all periods and equal to $(2\mu-1)^{1/2}$, where μ is ductility.

Keywords: Strength-reduction factors; Non-linear response; Earthquake motion near faults; Design of structures

1. Introduction

Engineering design of earthquake-resistant structures usually begins with pushover analyses (FEMA [1,2]; ATC [3]), which are scaled by target displacements determined from the inelastic response of the corresponding single-degree-of-freedom system (SDOF). Since the design ground motions are usually specified in terms of the response spectra of linear oscillators, this requires that the relationship between the peak relative displacement response, u_0, of the linear SDOF system and of its inelastic counterpart, u_m, be properly specified for the required design parameters and environment. By defining the yield strength-reduction factor as $R_y = u_0/u_y$, where u_y is the yielding displacement of the SDOF system equivalent spring, and ductility as $\mu = u_m/u_y$, for the same ground motion, the ratio u_m/u_0 is then equal to μ/R_y.

The relationship between the maxima of non-linear and linear responses of SDOF systems, u_m and u_0 (Fig. 1a), for the same excitation, has been studied extensively during the past 40 years. In one of the first studies by Veletsos and Newmark [4] it was shown that for a long-period SDOF system, when its natural period $T_n \to \infty$, $u_m/u_0 \to 1$ (equal deformation rule), and that for the response amplitudes governed mainly by the peak excitation velocities, $u_m/u_0 \to \mu/\sqrt{2\mu-1}$ (equal strain energy rule). With the gradual increase in the number of the recorded strong-motion accelerograms [5] these rules were further refined to reflect the trends observed in the responses to the recorded data [6–9] for different site conditions and ductility factors [10,11], for rupture distance and the earthquake magnitude [12], and for fault-normal near-field records in the zone affected by directivity [13,14]. For reinforced concrete structures, the range of T_n, where equal deformation rule applies was described by Shimazaki and Sozen [15], and it was suggested by Ruiz-Garcia and Miranda [16] that the average value of the ratio u_m/u_0 is not much influenced by the recording site classification, by earthquake magnitude, when $u_0/u_y < 4$ (u_y is yield deformation), or by rupture distance. Other studies have shown that u_m/u_0 for the high frequencies of the response (acceleration-sensitive region) are reduced by the postyield stiffness [17,18] and increased by stiffness degradation [18–20] and pinching of the hysteresis loop [21,22].

The weakness of many of the above-mentioned studies is that in a given paper only one or two governing parameters

*Corresponding author.
E-mail address: trifunac@usc.edu (M.D. Trifunac).

0267-7261/$ - see front matter © 2007 Elsevier Ltd. All rights reserved.
doi:10.1016/j.soildyn.2007.06.010

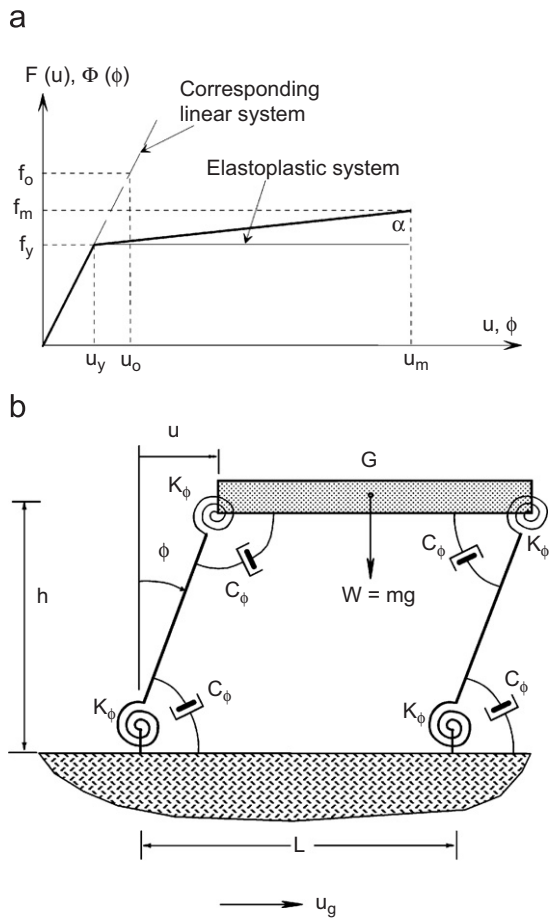

Fig. 1. (top) Force–displacement (moment–rotation) relationship for bi-linear spring. (bottom) Relative response, u, of the single-degree-of-freedom system excited by motion of rigid base, u_g.

are considered, with de facto averaging over all other parameters. Furthermore, the data set considered in most studies is not large enough to detect all significant dependencies with confidence. The exceptions to this trend can be found in two papers, one by Tiwari and Gupta [23] and the other by Chakraborti and Gupta [24]. Both papers present comprehensive regression models based on large data sets, and show the clear dependence of the strength-reduction factors on magnitude predominant period, duration of strong motion, and geologic site conditions.

In the near field of large earthquakes, and especially close to surface rupturing faults, the strong-ground motion can be dominated by the permanent displacements (typically parallel to the fault surface) and by large pulses (often perpendicular to the fault). Traces of these large displacements and pulses may not always be obvious in the processed records of the recorded motions because of the band-pass filtering, designed to eliminate digitization and processing noise [25–28]. This processing filters out the long-period ground displacements, and thus eliminates all permanent displacement components.

The purpose of this paper is to show how the strength-reduction factors depend on the amplitudes and duration of the near-fault pulses and displacements, in the conditions when these dominate the near-fault ground motion. The results should help in the selection of the correct design criteria for structures located in the vicinity of active faults and in the development of the regression equations for the strength-reduction factors when the distance between the site and the fault surface approaches zero. In general, the strength-reduction factors depend on the time history and the transient nature of the excitation, on the linear and non-linear characteristics of the SDOF system adopted for the analysis, and on the initial conditions. Since the recorded strong-motion data at or very close to the causative fault continue to be limited, the results of this study should help us understand how the known results for intermediate and far-field records of strong motion would change when extrapolated toward the fault rupture.

2. Near-source ground motion

Strong-ground motion near faults can be complicated due to irregular distribution of fault slip [25,29,30] because of non-uniform distribution of geologic rigidities surrounding the fault, non-uniform distribution of stress on the fault, and complex non-linear processes that accompany the faulting. Thus, in general, it is not possible to predict the detailed nature of the near-fault ground motion and of the associated pulses. In this paper we adopt a simplified approach and model these motions by smooth pulses, which have correct average amplitudes and duration, and which have been compared to and calibrated against the observed fault slip and the recorded strong motions in terms of their peak amplitudes in time and their spectral content [31,32].

Fig. 2 shows schematically a fault and two characteristic simple motions, d_N (Brune's near-field displacement) and d_F (Brune's far-field pulse), which describe monotonic growth of the displacement toward the permanent static offset, and a pulse, which near faults is usually perpendicular to the fault and associated with failure of a nearby asperity or passage of dislocation under or past the observation point [33].

For excitation by a pulse, we chose the Brune's "far-field" pulse (Fig. 2-center)

$$d_F(t) = A_F t e^{-\alpha_F t}, \tag{1}$$

where the values of A_F and α_F, for different earthquake magnitudes, are shown in Table 1 [31]. Since the strong-motion data are abundant only up to about $M = 6.5$, we place the values of α_F and A_F, for $M = 7$ and 8, in Tables 1 and 2 in parentheses to emphasize that those are based on extrapolation. For the near-field permanent displacement, we consider the Brune's displacement (Fig. 2-bottom)

$$d_N(t) = \frac{A_N}{2}(1 - e^{-(t/\tau_N)}), \tag{2}$$

where the values of A_N and τ_N, for different earthquake magnitudes, are shown in Table 2 [31].

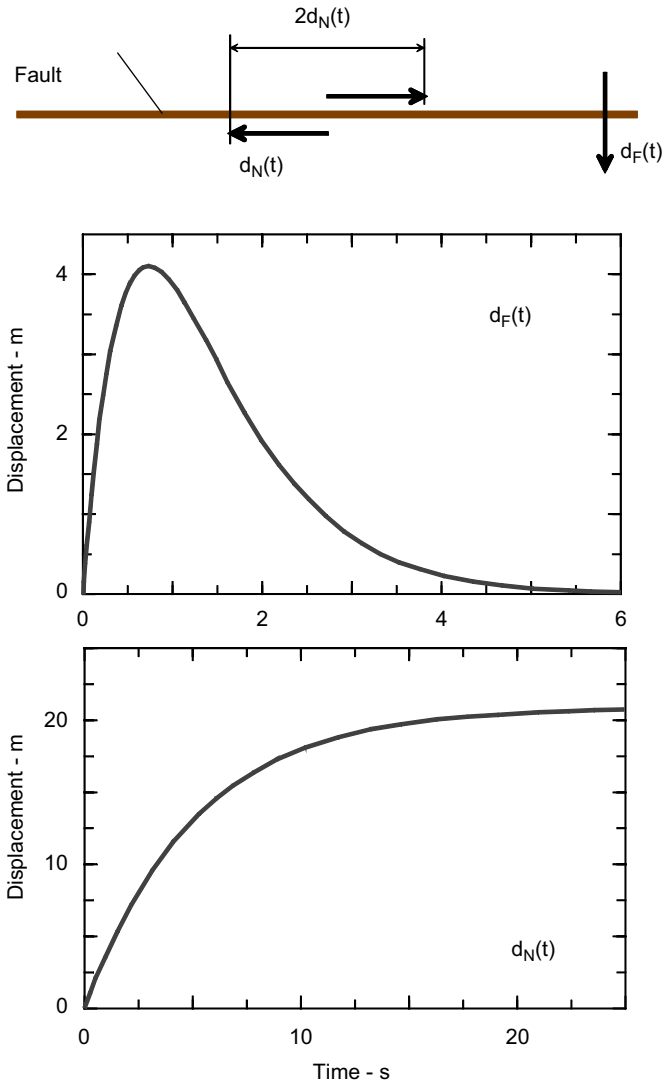

Fig. 2. Fault-parallel, $d_N(t)$, and fault-normal, $d_F(t)$, displacements.

Table 1
Characteristics of Brune's pulse displacement (Trifunac [31])

M (magnitude)	α_F (1/s)	A_F (cm/s)	$d_{F,max}$(cm)	$\dot{d}_{F,max}$(cm/s)
4	14.04	56.48	1.48	56.48
5	7.90	151.61	7.06	151.61
6	4.44	546.97	45.32	546.97
7	(2.50)	(860.34)	(126.6)	(860.34)
8	(1.40)	(1560.29)	(410.0)	(1560.29)

Table 2
Characteristics of Brune's near-field displacement (Trifunac [31])

M (magnitude)	τ_N (s)	A_N (cm)	$d_{N,max}$(cm)	$\dot{d}_{N,max}$(cm/s)
4	0.55	4.9	2.45	4.45
5	1.2	29.2	14.6	12.17
6	1.8	245.5	122.75	68.19
7	(3.0)	(1288.0)	(644.0)	(214.7)
8	(5.0)	(4169.0)	(2084.5)	(416.9)

The amplitudes of d_F and d_N have been studied in numerous regression analyses of recorded peak displacements at various distances from the fault and in terms of the observed surface expressions of fault slip. The latter are traditionally presented as average dislocation amplitudes, $\bar{u}$, and are related to d_N, as $\bar{u} = 2d_N$ (see Fig. 2 top). Fig. 3 (bottom shaded zone) shows, for example, the range of average ($p = 0.5$, where p is the probability of no excedance) peak ground displacements, d_{max}, versus magnitude, calculated at epicentral distance $R = 0$ km for the recording site conditions in the range from sediments ($s = 0$), to the basement rock ($s = 2$) [34]. The top gray zone shows the corresponding range for the 10% probability of being exceeded. The same figure also shows $d_{F,max}$ (see Table 1), the peak amplitudes of d_F used in this study. It is seen that the amplitudes of $d_{F,max}$ shown in Table 1 are consistent with extrapolations from the recorded strong-ground motion in the far field, and are close to d_{max} for $p = 0.5$ and $s = 0$, and $p = 0.9$ and $s = 2$.

Fig. 4 summarizes the trends of average dislocation amplitudes, $\bar{u} = 2d_N$, versus magnitude M. Average dislocation is the value of dislocation amplitudes averaged over the fault surface and is the quantity used in spectral interpretations of near-fault and near-field motions and of the body wave amplitudes in the far field. Various symbols show the results extracted from the studies of selected earthquakes [35,36,59], while the two gray zones outline the

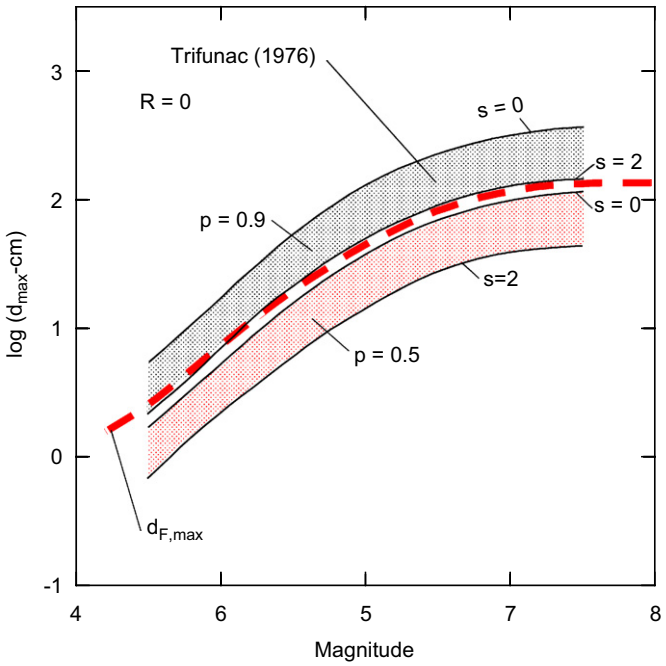

Fig. 3. Range of peak ground displacements, d_{max}, determined by regression analysis of recorded strong-ground motion. The dashed line shows $d_{F,max}$ (see Table 1). The bottom shaded zone gives the average ($p = 0.5$), while the top gray zone gives $d_{F,max}$ with amplitudes having 10% probability of being exceeded ($p = 0.9$). The width of the shaded zones describes variations associated with geological site conditions. The bottom of the zones is for $s = 2$ (basement rock), while the top is for $s = 0$ (sediments).

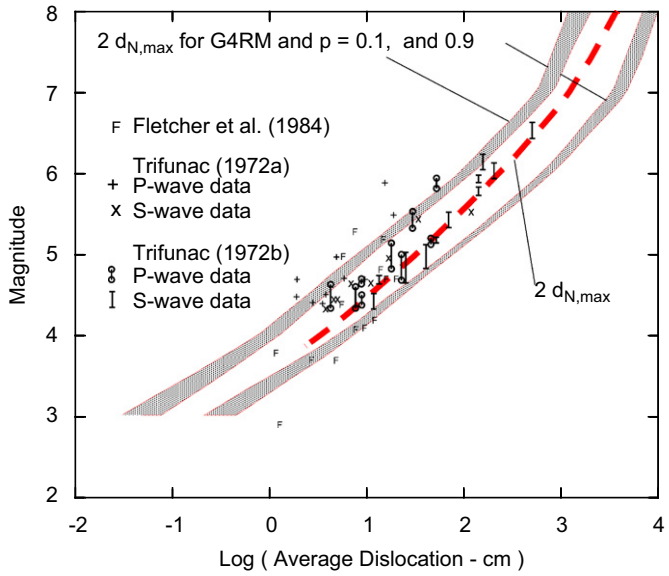

Fig. 4. Comparison of the distribution of the average dislocation amplitudes on the fault, $\bar{u} = 2d_{N,max}$, computed for the group of four regression models (G4RM), determined from the recorded strong-motion amplitudes (gray zones for $p = 0.1$ and 0.9), with the amplitudes of $d_{N,max}$ (Table 2), adopted for scaling $d_N(t)$ in this paper (dashed line).

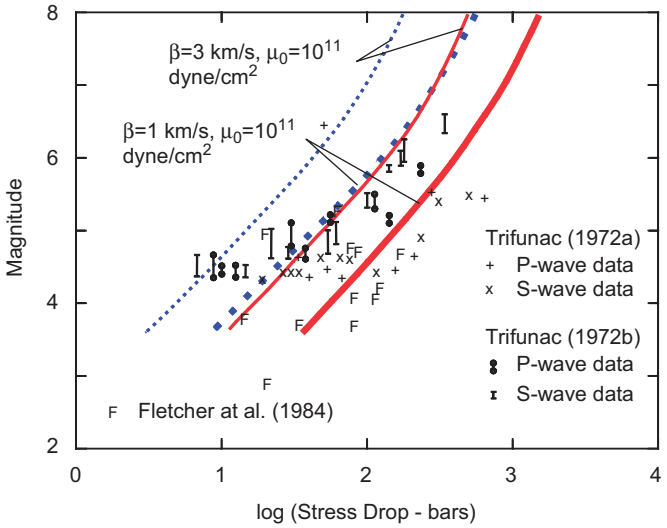

Fig. 5. Estimates of stress drop, from near-source recordings of strong motion, with the stress drop associated with $\dot{d}_F$ (solid lines, Table 1) and $\dot{d}_N$ (dotted lines, Table 2) used in this paper.

80% confidence interval (bounded by $p = 0.1$ and 0.9) for the amplitudes of $\bar{u} = 2d_N$ based on four regression models (G4RM), which describe attenuation of strong-motion amplitudes [31,37–40]. The dashed line shows the amplitudes of $2d_{N,max}$ as used in this paper (see Table 2). It is seen that the agreement is excellent.

An important physical property of the d_F and d_N functions, as used in this paper, is their initial velocity. It can be shown that $\dot{d}_F \sim \sigma\beta/\mu_s$, where σ is the effective stress ($\sim$ stress drop) on the fault surface [31,39], β is the velocity of shear waves in the fault zone, and μ_s is the rigidity of rocks surrounding the fault. For $\dot{d}_N$ it can be shown that $\dot{d}_F = 0.5C_0\sigma\beta/\mu_s$, at $t = 0$, where typical values of C_0 are 0.6, 0.65, 1.00, 1.52, and 1.52 for $M = 4$, 5, 6, 7, and 8 [31,39]. The largest peak velocities observed so far, are in the range of and exceed 200 cm/s (170 cm/s, 5–10 km above the fault of Northridge, California earthquake of 1994 [41], and 229 cm/s at station TCU068, near the end of surface expression of Che-lungpu fault, during Chi-Chi, Taiwan earthquake of 1999 [42]). Because there are no strong-motion measurements of peak ground velocity at the fault surface, the peak velocities $\dot{d}_F$ and $\dot{d}_N$ can be evaluated only indirectly in terms of σ. The accuracy of the stress estimates depends upon the assumptions and methods used in interpretation of recorded strong-motion records and is typically about one order of magnitude. Therefore, solving the above equations for σ we can use $\sigma \sim 2\mu_s\dot{d}_N/(\beta C_0)$ (dotted lines in Fig. 5) and $\sigma \sim \mu_s\dot{d}_F/\beta$ (continuous lines in Fig. 5), to check their consistency with other published estimates of σ [35,36,59]. Fig. 5 show this comparison for typical values of μ_s and β.

Since the dependence of both u_m/u_0 and the yield strength-reduction factor $R_y = u_0/u_y$, versus period T_n, are both functions of excitation and of the corresponding spectral amplitudes for the linear response, we next describe the PSV spectral amplitudes for $d_F(t)$ and $d_N(t)$ motions at the fault. Figs. 6a and b show the linear pseudo relative velocity (PSV) spectra computed for ground motions represented by d_F (Fig. 6a) and d_N (Fig. 6b), for magnitudes $M = 4$, 5, 6, 7, and 8, and for the fraction of critical damping $\zeta = 0.05$. In both figures, the role of large, non-zero initial velocity is evident. It dominates the amplitudes and the shape of PSV spectra, for both d_F and d_N excitations, with spectral amplitudes approaching constant asymptotes as $T_n \to 0$, whose amplitudes are equal to $\dot{d}_F$ and $\dot{d}_N$, respectively. At long periods, the corresponding relative displacement spectra, $SD = PSV/\omega_n$, approach the asymptotes whose amplitudes are equal to the peaks of d_F and d_N, $d_{F,max}$, and $d_{N,max}$, respectively. With increasing magnitude, the corner frequencies, which are direct functions of α_F and τ_N [31] progressively move toward longer periods. To enable a direct relative comparison of spectral amplitudes, and to emphasize how different the PSV spectral shapes are for d_F and d_N excitations, we superimpose in Figs. 6a and b the average PSV spectra estimated by regression analysis of more than 550 PSV spectral amplitudes computed from recorded accelerograms in the western US; they were recorded on sediments ($s = 0$) or on geological basement rock ($s = 2$), for a fraction of critical damping $\zeta = 0.05$, at "epicentral" distance $R = 0$ km, and for magnitudes $M = 4.5$, 5.5, 6.5, 7.5, and 8.5 [43].

Amplitudes of PSV spectra of the linear response of SDOF systems can be viewed, and scaled, in three period ranges, where the PSV amplitudes are proportional to (1) peak ground acceleration (short periods), (2) peak ground

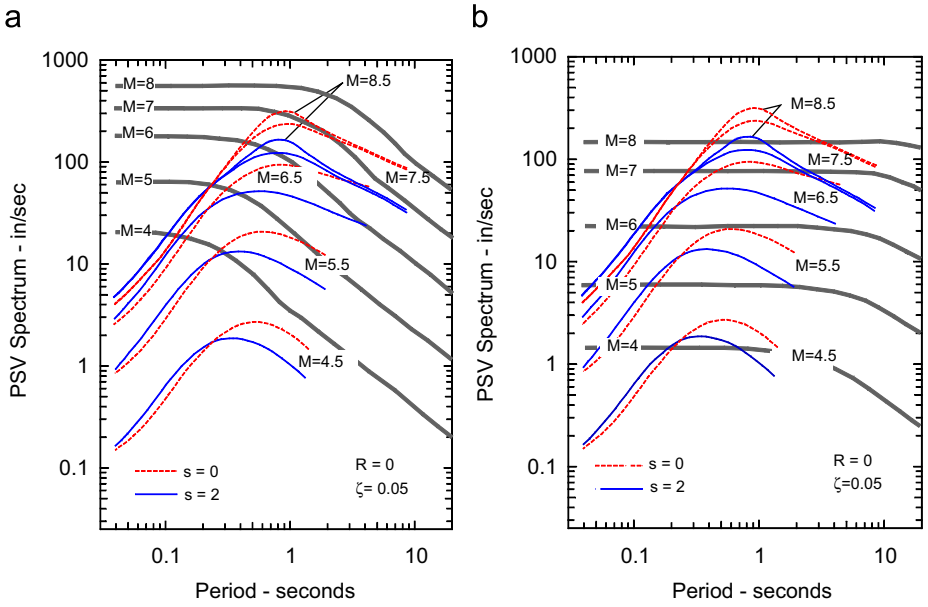

Fig. 6. (a) Comparison of PSV spectra for the pulse at the fault, $d_F(t)$ (wide lines), with average ($p = 0.5$) spectra of recorded strong-ground motion extrapolated to $R = 0$ km, for $\zeta = 0.05$, and for sites on basement rock ($s = 2$, solid lines), and on sediments ($s = 0$, dashed lines) (redrawn from Trifunac, [43]). (b) Same as Fig. 6a, but for excitation by the near-field displacement $d_N(t)$ (wide lines).

velocity (intermediate periods), and (3) peak ground displacement (long periods) [6]. As will be seen throughout this paper, when the motion begins with a sudden jump in ground velocity (caused by a sudden stress drop on the fault surface), this large initial velocity also dominates the spectral amplitudes for the short periods of the oscillator and the "acceleration-dominated" zone of PSV amplitudes disappears. This results in essentially constant PSV amplitudes in the short-period range.

We note that the effect of large initial velocities, $\dot{d}_F$ and $\dot{d}_N$, on the PSV spectral amplitudes in the short-period range is reminiscent of the effects of differential motions, particularly for stiff structures, at soft soil sites, and for large plan dimensions. There, the peak strains in the soil (proportional to peak ground velocity) lead to constant PSV spectral amplitudes at short periods [44,45].

The presence of the motions resembling d_N in the recorded velocities and displacements filtered by data processing will be noticed by a trained eye in numerous plots of processed strong-motion records [46]. The frequency of the occurrence and the amplitudes of such pulses are larger for the motions recorded closer to the causative faults. For the examples of d_F and d_N in this paper there is a Dirac delta function for accelerations at time zero. In the observed motions, because of wave propagation through sediments and soil, this will correspond to large but not infinite accelerations.

Fig. 7 (top) shows one of the early examples of the ground displacement, perpendicular to the fault, recorded during the Parkfield, California earthquake of 1966 [30]. This displacement, computed by double integration from the recorded accelerogram [47] is used here to illustrate the actual near-fault "pulse-like" ground motion, which in this

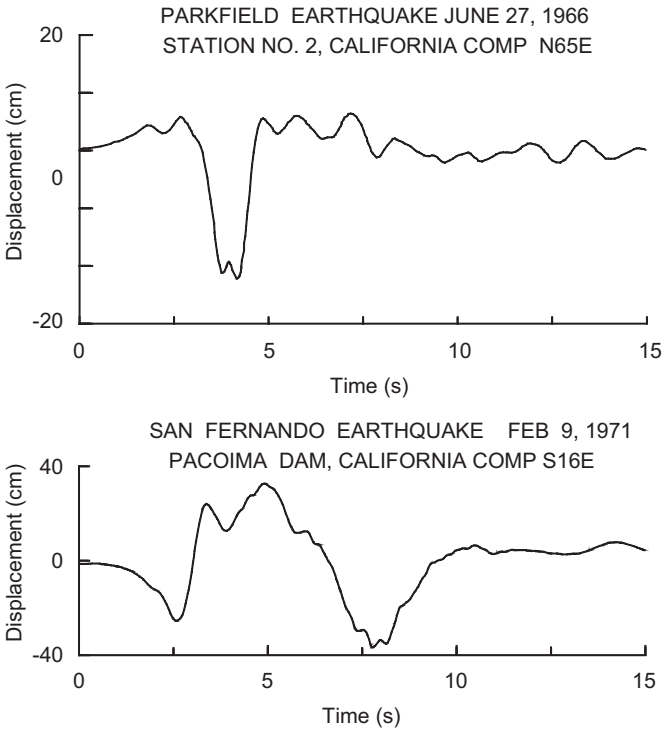

Fig. 7. (top) Ground displacement, perpendicular to the fault surface, near the end of the surface expression of a vertical strike-slip fault (redrawn from Housner and Trifunac, [47]). (bottom) Ground displacement recorded near center and above a thrust fault (Trifunac, [29]).

paper is modeled by d_F (shown in Fig. 2, middle). Fig. 7(bottom) shows the ground displacement computed during the San Fernando, California earthquake of 1971 [48]. This displacement has been high-pass filtered by the routine data processing methods [26], and therefore does

not contain periods of motion longer than 15 s. However in spite of the high-pass filtering it shows clearly two episodes of permanent ground displacements, starting near 2.5 and 7 s. Further examples of how d_N for this earthquake appeared near fault can be found in Figs. 6 and 10 of Trifunac [29], which are based on synthetic computation of the fault slip during the San Fernando earthquake of 1971.

3. Inelastic deformation ratio

The yield *strength-reduction factor* is $R_y = f_0/f_y = u_0/u_y$, where all the quantities are defined as in Fig. 1a. For ductility $\mu = u_m/u_y$, the *inelastic deformation ratio* u_m/u_0 is then equal to μ/R_y. The inelastic deformation ratio, for known yield strength, and same excitation $C_{R_y} = u_m/u_0 = \mu/R_y$, can be computed from calculated peak responses u_m and u_0. For given R_y, the associated ductility demand is then determined from μ/R_y. Iterations are required to compute the inelastic deformation ratio, $C_\mu = u_m/u_0$, for specified ductility factor because different values of f_y may lead to the same μ. Because C_μ is not unique, the convention is to choose the largest f_y corresponding to the largest C_μ [49].

For stiff, high-frequency oscillators, when $T_n \to 0$, the relative displacement of the mass, u, and its relative velocity, $\dot{u}$, are essentially zero. Then the absolute acceleration of the mass m is the same as the absolute acceleration of the ground $\ddot{u}_g$, and $f = -m\ddot{u}_g$, independent of the force-displacement relationship, and therefore $f_m \approx f_0$. From Fig. 1a it is seen that $f_y + (\mu - 1)\alpha f_y = f_m$, and when $f_m \approx f_0$, $1 + (\mu - 1)\alpha = R_y$. Then, as $T_n \to 0$, for $\alpha = 0$, $R_y \to 1$, and $u_m/u_0 \to \mu$. For $\alpha > 0$, R_y is larger than one, and $u_m/u_0 < \mu$.

For large initial velocity of ground motion, and for the oscillator periods, for which the response amplitudes are dominated by the peak amplitudes of ground velocity, equating the kinetic and potential energies of response leads to the requirement that the linear and non-linear oscillators, at the peaks of their responses, should have the same maximum strain energy. This leads to $f_0 u_0/2 = f_y u_y/2 + (u_m - u_y) f_y + \alpha(u_m - u_y)^2/2$ (see Fig. 1a). For $\alpha = 0$, this simplifies to $R_y = (2\mu - 1)^{1/2}$, and for $\mu = 1.5$, 2, 4, and eight $R_y = 1.41$, 1.73, 2.65, and 3.87, respectively. Then $u_m/u_0 = \mu(2\mu - 1)^{-1/2}$.

For long periods of the oscillator, when $T_n \to \infty$ and its stiffness approaches zero, both u_m and u_0 approach the negative of the peak ground displacement u_g, and then $u_m/u_0 \to 1$, and $R_y \to \mu$. This is known as the equal displacement rule [4].

4. Strength-reduction factor

Since the *inelastic deformation ratio* u_m/u_0 is equal to μ/R_y, for estimation of the non-linear response of an SDOF system, it suffices to describe the dependence of R_y versus T_n in terms of the parameters that characterize strong-ground motion and the physical characteristics of the structure (SDOF). The characteristics that will determine the nature of the strong-ground motion may include; for example, the size of the earthquake (usually in terms of a magnitude scale); geometry and the slip on the causative fault; the geometrical relationship between the site and the fault plane, usually expressed in terms of epicentral or some other characteristic distance; directivity; the nature of the medium between the source and the site; and the nature of the geological and soil conditions at the site. The characteristics of the SDOF system may include the nature

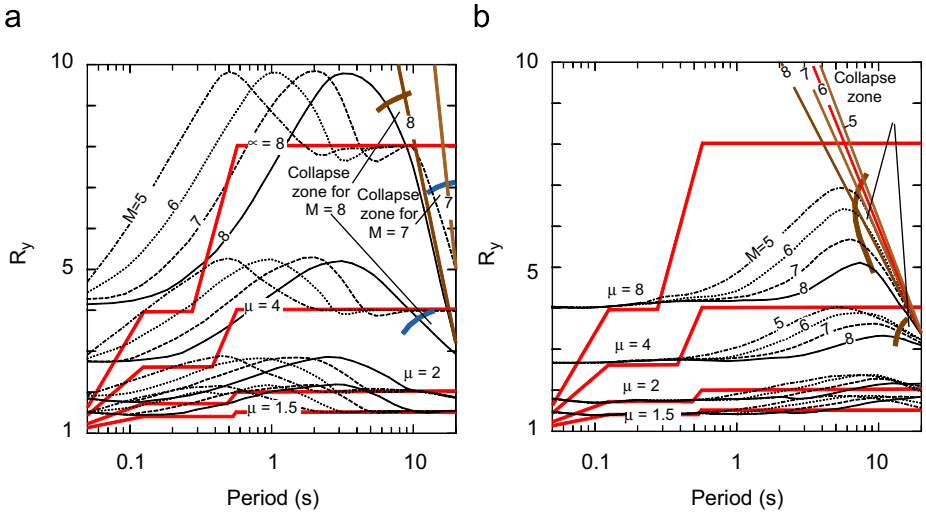

Fig. 8. (a) Comparison of strength-reduction factors computed for near-field pulse, $d_F(t)$, for $M = 5$, 6, 7, and 8, $\zeta = 0.05$, and $\mu = 1.5$, 2, 4, and 8 (continuous, dashed, dotted, and dash-dot lines), with piecewise straight representation of R_y based on the studies of Biggs, Elghadamsi, Hall, Lai, Mohraz, Riddell, and Hewmark (redrawn from Chopra, [50]). Above the wide lines, with negative slopes, for periods longer than about 10 s, the oscillators collapse, for $M = 7$ and 8. For long periods as R_y asymptotically move towards those lines from bellow, their amplitudes decrease, approaching the collapse zones. (b) Same as Fig. 8a, but for near-field displacement $d_N(t)$ (continuous, dashed, dotted, and dash-dot lines). In this figure, the collapse boundaries are shown for $M = 5$, 6, 7, and 8, and the collapse zones begin for periods longer than about 7 s and $\mu = 8$.

of its force displacement properties like degradation of stiffness in terms of the number of cycles and amplitudes of the response, pinching of the hysteresis loop, consequences of geometric non-linearities, the effects of gravity, dynamic instability, coupling of the response to multi-component excitation, and so on.

With the gradual increase in the number of the recorded and processed strong-motion accelerograms, the dependence of R_y versus T_n could be investigated using the computed non-linear response first from several and then from several hundred strong-motion records (e.g.), [4,12,14]. Piecewise straight segments of thick lines in Figs. 8 show a typical example of R_y versus period T_n, for $\mu = 1.5$, 2, 4, and 8. R_y is equal to 1 for $T_n < T_a$, to $(2\mu-1)^{1/2}$ for $T_b < T_n < T_c$, and to μ for $T_n > T_c$, where on firm ground $T_a = 1/33$, $T_b = 1/8$, and $T_c = 0.55$ s in this example, but in general depends on damping. This example, taken from Chopra [50], is based on and is representative of the studies by Biggs, Elghadamsi, Hall, Lai, Mohraz, Riddell, and Newmark [51,52,53]. The sloping straight lines provide transition between the two constant segments and $R_y = 1$ for $T_n \to 0$. The trends of R_y versus T_n, shown in Figs. 8, are average trends based on the computation of non-linear response to a small number of recorded strong-motion records and ignore any dependence on earthquake magnitude, source to site distance, or local site conditions.

Irregular thick lines, for $\mu = 2$ and 4, in Figs. 9, redrawn from MacRae et al. [14], show R_y versus period T_n, for average strike-normal records at distances of 20–30 km from epicenter, in the direction of rupture propagation, for closest distance to rupture 0–10 km, and for fraction of critical damping equal to 2%. Those are compared with R_y computed for the near-fault pulse d_F (Fig. 9a) and for the near-fault displacement d_N (Fig. 9b). MacRae et al. [14] analyzed 154 earthquake records and reported that the directivity effects cause a more severe response only for periods T_n between 1 and 3 s. Their results showed no significant dependence of R_y versus period T_n on earthquake magnitude.

Smooth wide lines in Figs. 10, for $\mu = 1.5$, 2, and 4, redrawn from Krawinkler and Nassar [54] show R_y versus period T_n curves, which have been used in several other studies [55–58]. As in many other previous studies, the dependence of R_y on earthquake magnitude is assumed to be small and hence is not considered.

The purpose of Figs. 8–10 here is to illustrate the range of the variations in the shape of R_y versus period T_n functions, based on different subsets of the recorded strong-motion data, and to contrast those shapes with the ones computed in this paper for near-fault pulse and near-fault displacement.

5. Strength-reduction factors for near-fault motions d_F and d_N

We computed the relative response, $u = h \sin\phi$, of an SDOF system (Fig. 1b) consisting of a rigid mass of length L supported by two rigid mass-less columns, which are connected at the top to the mass by circular springs and at the bottom also by circular springs to the ground. The stiffness of the springs is assumed to be elastic–plastic, as shown in Fig. 1a, with $\alpha = 0$. The massless columns are

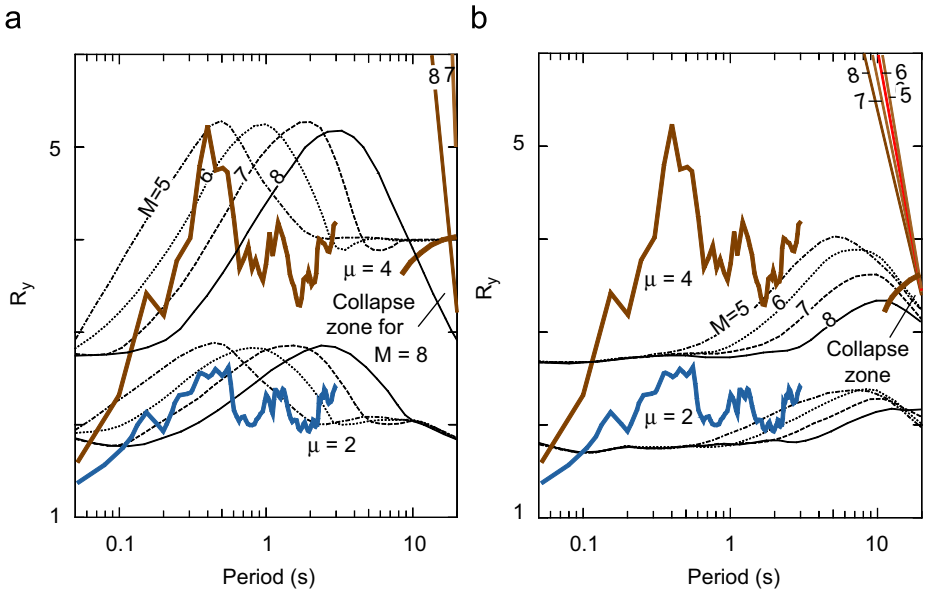

Fig. 9. (a) Comparison of strength-reduction factors computed for near-field pulse, $d_F(t)$, for $M = 5$, 6, 7, and 8, and $\mu = 2$ and 4 (continuous, dashed, dotted, and dash-dot lines), with R_y computed by MacRae et al. [14] for 154 earthquake records, for epicentral distances less than 30 km, in the direction of rupture propagation, and for $\zeta = 0.02$ (irregular wide lines). The collapse boundaries for $M = 7$ and 8, and the collapse zone for $M = 8$ appear for periods longer than about 10 s, and for $\mu = 4$. (b) Same as Fig. 9a, but for R_y computed for near-field displacement $d_N(t)$ (continuous, dashed, dotted, and dash-dot lines). The collapse boundaries for $M = 5$, 6, 7 and 8, and the corresponding collapse zones appear for periods longer than about 10 s, and for $\mu = 4$.

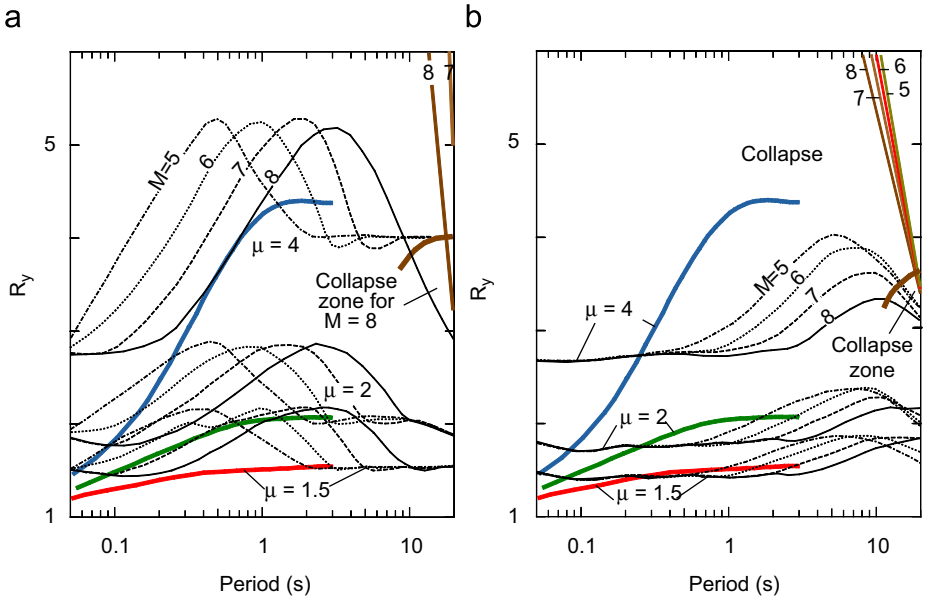

Fig. 10. (a) Comparison of strength-reduction factors computed for near-field pulse, $d_F(t)$, for $M = 5$, 6, 7, and 8, $\zeta = 0.05$, and $\mu = 1.5$, 2, 4, and 8 (continuous, dashed, dotted, and dash-dot lines), with R_y (wide lines) computed by Krawinkler and Nassar [54]. The collapse boundaries for $M = 7$ and 8, and the collapse zone for $M = 8$ appear for periods longer than about 10 s, and for $\mu = 4$. (b) Same as Fig. 10a, but for R_y computed for near-field displacement $d_N(t)$ (continuous, dashed, dotted, and dash-dot lines). The collapse boundaries for $M = 5$, 6, 7 and 8, and the corresponding collapse zones appear for periods longer than about 10 s, and for $\mu = 4$.

connected to ground and to the rigid mass by circular dashpots providing the fraction of critical damping equal to 5%. Rotation of the columns is assumed not to be small, which leads us to consider the geometric non-linearities. The mass is acted upon by the acceleration of gravity, g, and is excited by the horizontal ground acceleration, $\ddot{u}_g$, at its base. The functional form of $\ddot{u}_g$ is defined by the second derivative with respect to time of the near-fault displacements d_F and d_N, as in Eqs. (1) and (2), respectively. The governing differential equation for the SDOF system in Fig. 1b is then

$$\ddot{\phi} + 2\omega_n \varsigma \dot{\phi} + \Phi(\phi)/mh^2 - (g/h)\sin\phi = -(\ddot{u}_g/h)\cos\phi, \quad (3)$$

where when $\alpha = 0$ (Fig. 1a),

$$\Phi(\phi) = \begin{cases} k\phi & \text{when} \quad |\phi| < \phi_y \\ \pm k\phi_y & \text{when} \quad \phi > \phi_y \quad \text{or} \quad -\phi < -\phi_y \end{cases} \quad (4)$$

and $u_y = h\sin\phi_y$, as in Fig. 1a.

When ϕ is small, Eq. (3) reduces to

$$\ddot{\phi} + 2\omega_n \varsigma \dot{\phi} + \omega_n^2(1 - gmh/k)\phi = -\ddot{u}_g/h, \quad (5)$$

where $\omega_n^2 = k/(mh^2)$, and g is acceleration of gravity.

In the presence of gravity, the SDOF system is stable when $\phi < \phi_s$, and ϕ_s is determined from

$$\Phi(\phi_s) = hmg\sin\phi_s. \quad (6)$$

At $\phi = \phi_s$, the overturning moment by gravity force $hmg\sin\phi_s$is equal to the restoring moment in the helical springs $\Phi(\phi_s)$. For simplicity, and to save computer time, we assume that the system will collapse when $\phi > \phi_s$.

It is seen that for large excitation amplitudes, this structure will experience permanent distortions and may collapse. In all calculations we consider simultaneous action of the effects of gravity forces, dynamic instability, and geometric non-linearities. For this structure, we calculate u_m and u_0, for d_F and d_N corresponding to earthquake magnitudes $M = 5$, 6, 7, and 8, for ductilities $\mu = 1.5$, 2, 4, and 8, and then plot R_y versus T_n. We overlay the results in Figs. 8 through 10 for comparison with previous studies on how R_y depends upon T_n. In Figs. 8a, 9a, and 10a we show our results for R_y versus T_n for excitation by the pulse d_F (Fig. 2 center), and in Figs. 8b, 9b, and 10b for excitation by the near-fault displacement d_N (Fig. 2 bottom).

In Figs. 8a through 10b, for periods T_n in the vicinity and longer than about 10 s, the amplitudes of R_y become sensitive to action of the gravity load. There, for large magnitudes and ductilities, R_y dips to smaller amplitudes, below the constant asymptotes equal to μ. There, the destabilizing effect of gravity and of horizontal excitation lead to conditions that are close to collapse ($\phi > \phi_s$). In Figs. 8a through 10b, for$\mu > 4$ the values of R_y for which collapse occurs are shown by almost straight lines with negative slopes, asymptotically approaching R_y curves from above. In the zones labeled "Collapse zone," only minor increases in R_y will lead to collapse.

The classical strength-reduction factors equal to μ for T_n longer than about 0.5 s, and to $(2\mu-1)^{1/2}$ for periods between about 0.1 and 0.4 s (Fig. 8a), compare favorably with our calculations and would be conservative if used with near-fault excitation d_F, except for short intervals in T_n and for $M = 8$. For all other magnitudes our results are

above μ or $(2\mu-1)^{1/2}$. For short periods, our results for R_y tend to an asymptote with amplitude equal to $(2\mu-1)^{1/2}$, which is a consequence of strong initial velocities associated with a sudden onset of d_F. Such behavior is observed even when non-linearity is not present, as can be seen in Fig. 6 for PSV spectra of d_F and d_N.

Fig. 9a shows similarity in the trends of our results for $M=5$ with average trends presented by MacRae et al. [14]. Because their results show average trends, and because most of their strong-motion data are for magnitudes less than 7, it is possible to argue that their results reflect a presence of strong-motion pulses corresponding to the failure of single asperities for earthquakes less than about 5, and of multiple asperities for larger-magnitude events. The physics behind this reasoning is described in two papers by Trifunac [31,39]. His studies of spectral characteristics of the recorded strong motion in California, as viewed in the frequency range of interest for engineering (say 0.1–25 Hz), suggest that most earthquakes smaller or equal to about $M=5$, could be viewed as failures of one asperity, while the larger events can be viewed as failures involving multiple asperities (with indicative numbers of 3, 15, and 90 asperities, for $M=6$, 7, and 8).

Our results for R_y versus T_n also agree qualitatively with those of Krawinkler and Nassar [54], shown in Fig. 10a, except that their results would not be conservative if used for near-fault pulses when T_n is longer than about 1 s. In Figs. 8b, 9b and 10b, for periods T_n longer than about 0.2–0.4 s, and for ductilities 4 and 8, the traditional design curves illustrated here [14,50,54] are not conservative.

6. Discussion and conclusions

We have described the variations in the strength-reduction factor, R_y versus T_n, for different earthquake magnitudes, M, for typical motions on the surface fault, modeled using the near-fault displacement pulse, d_F, characteristic of the fault-normal displacements, and the permanent displacement, d_N, which describes fault-parallel motions. We found strong dependence of R_y versus T_n on magnitude. These results are different and contradict the conclusions of many previous studies, which typically found little or no dependence in R_y versus T_n on magnitude. Our results are in qualitative agreement with those presented by Tiwari and Gupta [23] and Chakraborti and Gupta [24]. These observed differences can be explained by the nature of the physical process in question. The large static and dynamic parts of the near-fault ground motions, which occur near the moving faults, can be shown to decay rapidly with distance from the fault, Δ, as Δ^{-4} and Δ^{-2} [33] and therefore become small relative to the body and surface waves for Δ larger than 1–2 source dimensions [29,31]. The study by Mac Rae et al. [14], however, was able to detect the dependence on directivity of fault-normal versus fault-parallel strong motion for a selected group of strong-motion records for "small" fault-to-station distances. Their average trend for R_y versus T_n curves is also consistent with the results of this study, if we assume that typical multiple asperities broken by the larger magnitude events (e.g. larger than 6) are representative of approximately magnitude 5 events [31,39].

Our results show that the average trends of most R_y versus T_n curves used in the design are conservative for pulse-like fault-normal motions near faults, which we modeled in this paper by d_F. However the same design curves are not conservative for fault-parallel motions, modeled in this paper by d_N, and for periods T_n longer than about 0.2–0.4 s. The simple remedy for this problem is to replace the strength-reduction factors by $(2\mu-1)^{1/2}$ for all periods T_n, for all designs near faults.

Most previous studies of the strength-reduction factors show $R_y=1$ when $T_n\to 0$. This results from the common assumption that for stiff, high-frequency oscillators, when $T_n\to 0$, the relative displacement of the mass, u, and its relative velocity, $\dot{u}$, are essentially zero. Also, in the response analyses of linear and non-linear response of SDOF systems excited by the recorded strong-motion accelerograms it is assumed that the initial conditions for u and $\dot{u}$ are sufficiently small, so that those can be approximated by zero. Our selection of the functional forms for d_F and d_N leads to large initial strong-motion velocities at $t=0$, which result from the physical nature of ground motion caused by sudden stress drop on the fault surface [31,39]. As can be seen from the results presented in Figs. 8 through 10, this causes our R_y versus T_n curves to not converge to $R_y=1$ when $T_n\to 0$, but to an asymptote with an amplitude of $(2\mu-1)^{1/2}$. For the near-fault fault-parallel displacement, d_N, this initial velocity dominates the relative response for virtually all periods.

In summary, the results of this study suggest that for conservative design of structures near faults the simple and effective modification of the strength-reduction curves would be to replace the current values for R_y versus T_n by a constant equal to $(2\mu-1)^{1/2}$, for both fault-normal and fault-parallel motions. This is because in nature the faults are rarely straight and regular surfaces, and so it is difficult to predict when the near-fault motions will follow closely the examples of d_F and d_N employed in our study. Thus, it would be conservative to use the strength-reduction factor $(2\mu-1)^{1/2}$ for all near-fault motions, irrespective of their orientation.

Acknowledgments

We are indebted to Prof. V.K. Gupta of IIT Kanpur, and to one anonymous reviewer for critical reading of the manuscript, and for offering many useful suggestions that led to significant improvement of the paper.

References

[1] Federal Emergency Management Agency (FEMA). NEHRP guidelines for the seismic rehabilitation of buildings. Report no.

FEMA-273 (Guidelines) and report no. FEMA-274 (Commentary), Washington, DC, 1997.
[2] Federal Emergency Management Agency (FEMA). Prestandard and commentary for seismic rehabilitation of buildings. Report no. FEMA-356, Washington, DC, 2000.
[3] Applied Technology Council (ATC), Seismic evaluation and retrofit of concrete buildings. Report no. ATC-40, Redwood City, California, 1996.
[4] Veletsos AS, Newmark NM. Effect of inelastic behavior on the response of simple systems to earthquake motions. In: Proceedings of the second world conference on earthquake engineering, vol. II, 1960, pp. 859–912.
[5] Trifunac MD, Todorovska MI. Evolution of accelerographs, data processing, strong motion arrays and amplitude and spatial resolution in recording strong earthquake motion. Soil Dyn Earthquake Eng 2001;21(6):8537–55.
[6] Veletsos AS, Newmark NM, Celapati CV. Deformation spectra for elastic and elastoplastic systems subjected to ground shock and earthquake motion. In: Proceedings of the third world Conference on earthquake engineering, Wellington, New Zealand, vol. II, 1965, pp. 663–82.
[7] Veletsos AS, Vann WP. Response of ground-excited elastoplastic systems. J Struct Div ASCE 1971;97(4):1257–81.
[8] Chopra AK, Chintanapakdee C. Comparing response of SDOF systems to near-fault motions in the context of spectral regions. Earthquake Eng Struct Dyn 2001;30(12):1769–89.
[9] Riddell R, Garcia J, Garces E. Inelastic deformation response of SDOF systems subjected to earthquakes. Earthquake Eng Struct Dyn 2002;31(3):515–38.
[10] Miranda E. Seismic evaluation and upgrading of existing structures. PhD thesis, University of California at Berkeley, Berkeley, CA, 1991.
[11] Ruiz-Garcia J, Miranda E. Inelastic displacement ratios for evaluation of structures built on soft soil sites. Earthquake Eng Struct Dyn 2006;35(6):679–94.
[12] Miranda E. Inelastic displacement ratios for structures on firm sites. J Struct Eng 2000;126(10):1150–9.
[13] Baez JI, Miranda E. Amplification factors to estimate inelastic displacement demands for the design of structures in the near field. In: Proceedings of 12th world conference on earthquake engineering, (CD-Rom), Auckland, New Zealand, 2000.
[14] MacRae GA, Morrow DV, Roeder CW. Near-fault ground motion effects on simple structures. J Struct Eng 2001;127(9): 996–1004.
[15] Shimazaki K, Sozen MA. Seismic drift of reinforced concrete structures. Technical research report prepared for Hazama-Gumi Ltd., Tokyo, 1984, pp. 145–66.
[16] Ruiz-Garcia J, Miranda E. Inelastic displacement ratios for evaluation of existing structures. Earthquake Eng Struct Dyn 2003;32(8): 1237–58.
[17] Veletsos AS. Maximum deformation of certain nonlinear systems. In: Proceedings of the fourth world conference on earthquake engineering, Santiago, Chile, vol. II, 1969, A4-155-A4-170.
[18] Qi X, Moehle JP. Displacement design approach for reinforced concrete structures subjected to earthquakes. Report no. EERC-91/02, Earthquake Engineering Center, U. California at Berkeley, Berkeley, CA, 1991.
[19] Clough RW. Effect of stiffness degradation on earthquake ductility demands. Report no. SEMM 66-16, Department of Civil Engineering, University of California at Berkeley, Berkeley, CA, 1966.
[20] Song JK, Pincheira JA. Spectral displacement demands of stiffness- and strength-degrading systems. Earthquake Spectra 2000;16(4): 817–51.
[21] Gupta A, Krawinkler H. Effect of stiffness degradation on deformation demands for SDOF and MDOF structures. In: Proceedings of the sixth national conference on earthquake engineering, Earthquake Engineering Institute, Oakland, CA, 1998.
[22] Gupta A, Kunnath S. Effect of hysteretic model parameters on inelastic system demands. In: Proceedings of the sixth national conference on earthquake engineering, Earthquake Engineering Research Institute, Oakland, CA, 1998.
[23] Tiwari AK, Gupta VK. Scaling of ductility and damage-based strength reduction factors for horizontal motions. Earthquake Eng Struct Dyn 2000;29(7):969–87.
[24] Chakraborti A, Gupta VK. Scaling of strength reduction factors for degrading elasto-plastic oscillators. Earthquake Eng Struct Dyn 2005;34(2):189–206.
[25] Mavroeidis GP, Dong G, Papageorgiou AS. Near-fault ground motions, and the response of elastic and inelastic single-degree-of-freedom (SDOF) systems. Earthquake Eng Struct Dyn 2004;33(9): 1023–49.
[26] Trifunac MD, Lee VW. Routine computer processing of strong-motion accelerograms. Earthquake Engineering Research Laboratory, EERL 73-03, California Institute of Technology, Pasadena, CA, 1973.
[27] Trifunac MD, Lee VW. Automatic digitization and processing of strong-motion accelerograms. Part I-pp. 1–259, Part II pp. 260–379, Department of Civil Engineering, Report CE 79-15, University of Southern California, Los Angeles, CA, 1979.
[28] Boore DM, Bommer JJ. Processing strong-motion accelerograms: needs, options and consequences. Soil Dyn Earthquake Eng 2005;25(2):93–115.
[29] Trifunac MD. A Three-dimensional dislocation model for the San Fernando, California, earthquake of February 9, 1971. Bull Seismol Soc Am 1974;64(1):149–72.
[30] Trifunac MD, Udwadia FE. Parkfield, California, earthquake of June 27, 1966: a three-dimensional moving dislocation. Bull Seismol Soc Am 1974;64(3):511–33.
[31] Trifunac MD. Broad band extension of Fourier amplitude spectra of strong motion acceleration, Department of Civil Engineering. Report CE 93-01, University of Southern California, Los Angeles, CA, 1993.
[32] Trifunac MD, Todorovska MI. Broad band extension of pseudo relative velocity spectra of strong motion, Department of Civil Engineering. Report CE 94-02, University of Southern California, Los Angeles, CA, 1994.
[33] Haskell NA. Elastic displacements in the near field of a propagating fault. Bull Seismol Soc Am 1969;59(2):956–80.
[34] Trifunac MD. Preliminary analysis of the peaks of strong earthquake ground motion–dependence of peaks on earthquake magnitude, epicentral distance, and recording site conditions. Bull Seismol Soc Am 1976;66(1):189–219.
[35] Trifunac MD. Stress estimates for San Fernando, California earthquake of February 9, 1971: main event and thirteen aftershocks. Bull Seismol Soc Am 1972;62(3):721–50.
[36] Trifunac MD. Tectonic stress and source mechanism of the Imperial Valley, California earthquake of 1940. Bull Seismol Soc Am 1972;62(5):1283–302.
[37] Trifunac MD. Fourier amplitude spectra of strong motion acceleration: extension to high and low frequencies. Earthquake Eng Struct Dyn 1994;23(4):389–411.
[38] Trifunac MD. Response spectra of strong motion acceleration: extension to high and low frequencies. In: Proceedings of the 10th European conference on earthquake engineering, Balkema, Rotterdam, 1995, pp. 203–8.
[39] Trifunac MD. Stresses and intermediate frequencies of strong motion acceleration. Geofizika 1998;14:1–27.
[40] Trifunac MD. The role of the Brune spectrum in earthquake engineering. J Seismol Earthquake Eng 2005;7(2):63–82.
[41] Trifunac MD, Todorovska MI, Lee VW. The Rinaldi strong motion accelerogram of the Northridge, California, earthquake of 17 January, 1994. Earthquake Spectra 1998;14(1):225–39.
[42] Chen K-C, Huang B-S, Wang J-H, Huang W-G, Chang T-M, Hwang R-D, et al. An observation of rupture pulses of the 20 September 1999 Chi-Chi, Taiwan, earthquake from near-field seismograms. Bull Seismol Soc Am 2001;91(5):1247–54.
[43] Trifunac MD. Response spectra of earthquake ground motion. J Eng Mech Div ASCE 1978;104(EM5):1081–7.

[44] Trifunac MD, Todorovska MI. Response spectra and differential motion of columns. Earthquake Eng Struct Dyn 1997;26(2):251–68.
[45] Gicev V, Trifunac MD. Response spectra for differential motion of columns, paper II: out-of-plane response. Soil Dyn Earthquake Eng 2006;26(2):1149–60.
[46] Trifunac MD, Lee VW. Uniformly processed strong earthquake ground accelerations in the western United States of America for the period from 1933 to 1971: corrected acceleration, velocity and displacement curves, Department of Civil Engineering. Report CE 78-01. University of Southern California, Los Angeles, CA, 1978.
[47] Housner GW, Trifunac MD. Analysis of accelerograms–parkfield earthquake. Bull Seismol Soc Am 1967;57(6):1193–220.
[48] Trifunac MD, Hudson DE. Analysis of the pacoima dam accelerogram, San Fernando, California earthquake of 1971. Bull Seismol Soc Am 1971;61(5):1393–411.
[49] Veletsos AS, Newmark NM. Response spectra for single-degree-of-freedom elastic and inelastic systems. Report no. RTD-TDR-63-3096, vol. III, Air Force Weapons Laboratory, Albuquerkque, NM, 1964.
[50] Chopra AK. Dynamics of structures: theory and applications to earthquake engineering. New Delhi: Prentice-Hall of India; 1996.
[51] Elghadamsi FE, Mohraz B. Inelastic earthquake spectra. J Earthquake Eng Struct Dyn 1987;15(1):91–104.
[52] Lai SP, Biggs JM. Inelastic response spectra for aseismic building design. J Struct Div ASCE 1980(No. ST6):1295–310.
[53] Riddell R, Newmark NM. Statistical analysis of the response of nonlinear systems subjected to earthquakes, Civil engineering studies, Structural research series 468, Department of Civil Engineering, University of Illinois, Urbana, IL, 1979.
[54] Krawinkler H, Nassar AA. Seismic design based on ductility and cumulative damage demands and capacities. In: Fajfar P, Krawinkler H, editors. Nonlinear seismic analysis and design of reinforced concrete buildings. New York: Elsevier Applied Science; 1992.
[55] Miranda E, Bertero VV. Evaluation of strength reduction factors for earthquake resistant design. Earthquake Spectra 1994;10(2):357–79.
[56] Reinhorn AM. Inelastic analyses techniques in seismic evaluations. In: Fajfar P, Krawinkler H, editors. Seismic design methodologies for the next generation of codes. Rotterdam, The Netherlands: Balkema; 1997. p. 277–87.
[57] Chopra AK, Goel RK. Capacity-demand-diagram methods based on inelastic design spectrum. Earthquake Spectra 1999;15(4):637–56.
[58] Miranda E. Estimation of inelastic deformation demands for SDOF and MDOF systems. J Struct Eng 2001;127(9):1005–12.
[59] Fletcher J, Boatwright J, Haar L, Hanks T, McGarr A. Source parameters for aftershocks of the Oroville, California, Earthquake. Bull Seismol Soc Am 1984;74(4):1101–23.